Multiconfigurational study of the negatively charged nitrogen-vacancy center in diamond

Churna Bhandari , ^{1,*} Aleksander L. Wysocki , ¹ Sophia E. Economou, ¹ Pratibha Dev , ² and Kyungwha Park , ^{1,†} ¹Department of Physics, Virginia Tech, Blacksburg, Virginia 24061, USA

²Department of Physics and Astronomy, Howard University, Washington, District of Columbia 20059, USA

(Received 10 October 2020; revised 5 January 2021; accepted 8 January 2021; published 25 January 2021)

Deep defects in wide band gap semiconductors have emerged as leading qubit candidates for realizing quantum sensing and information applications. Due to the spatial localization of the defect states, these deep defects can be considered as artificial atoms/molecules in a solid state matrix. Here we show that unlike single-particle treatments, the multiconfigurational quantum chemistry methods, traditionally reserved for atoms/molecules, accurately describe the many-body characteristics of the electronic states of these defect centers and correctly predict properties that single-particle treatments fail to obtain. We choose the negatively charged nitrogenvacancy (NV⁻) center in diamond as the prototype defect to study with these techniques due to its importance for quantum information applications and because its properties are well known, which makes it an ideal benchmark system. By properly accounting for electron correlations and including spin-orbit coupling and dipolar spin-spin coupling in the quantum chemistry calculations, for the NV⁻ center in diamond clusters, we are able to: (i) show the correct splitting of the ground (first-excited) spin-triplet state into two levels (four levels), (ii) calculate zero-field splitting values of the ground and excited spin-triplet states, in good agreement with experiment, (iii) determine many-body configurations of the spin-singlet states, and (iv) calculate the energy differences between the ground and exited spin-triplet and spin-singlet states, as well as their ordering, which are also found to be in good agreement with recent experimental data. The numerical procedure we have developed is general, and it can screen other color centers whose properties are not well known but promising for applications.

DOI: 10.1103/PhysRevB.103.014115

I. INTRODUCTION

Defects in solid-state systems are naturally formed and can be implanted in a controllable fashion. Individual defects deeply embedded in wide band-gap semiconductors are known to have distinct localized electronic states within the band gap and so they behave similar to atoms or molecules. The prototype of such deep defects is the negatively charged nitrogen-vacancy (NV⁻) center defect in diamond which has been extensively used for sensing [1,2], for the demonstration of loophole-free Bell inequalities [3], and for a proof of principle of quantum error correction [4,5], to name a few among many important experiments and quantum information science applications. Its tremendous success was culminated in recent experimental realization of quantum entanglement between the spins of the NV⁻ centers over a kilometer range [3]. Single spins of the NV⁻ center defects were shown to be optically initialized and read out with long spin-lattice relaxation and spin coherence times at room temperature [6–13], and the electronic spin can be coherently controlled both optically [14] and via microwave fields [15]. This prototype defect inspired exploration of other defects, hopefully even more suitable for quantum information science applications, in diamond and other wide band-gap semiconductors such as the silicon vacancies and NV center in silicon carbide [16–20],

the silicon vacancy center in diamond [21–25], and rare-earth defects in silicon [26] or yttrium orthosilicate [27].

Electronic and magnetic properties of deep defects have been studied using either various levels of ab initio theory or phenomenological molecular models based on group theory. In the quest of unexplored, improved defects, ab initio theory rather than the molecular model approach can play an essential role in screening candidate defects for quantum information science applications before experimental data are available, because the latter approach requires parameter values such as Coulomb interactions and dipolar spin-spin coupling (SSC) and spin-orbit coupling (SOC) strengths. To that end, the techniques need to be reliable and predict defect properties as accurately as possible. Although single-particle ab initio techniques are extensively used, they have serious limitations for strongly correlated systems, especially for excited states. For example, density-functional theory (DFT) (as well as the molecular model approach) could not correctly predict the ordering of the spin-singlet states of the NV⁻ center defect in diamond [28-31], which led to a longstanding debate and conflicting results in the community [30-34]. Recent experimental results resolved this conflict [35-37]. Furthermore, DFT could not correctly predict either the ordering or the energy difference between the excited spin-triplet and spin-singlet states of the NV- center defect [28,38,39]. The aforementioned incorrect predictions of DFT highly influence our understanding of optical transitions between the triplet and singlet states referred to as intersystem crossings [6,30,33,34], which are key mechanisms to initialize and readout the spin-polarized states for quantum technology applications.

^{*}Current address: The Ames Laboratory, U.S. Department of Energy, Iowa State University, Ames, Iowa 50011, USA.

[†]Corresponding author: kyungwha@vt.edu

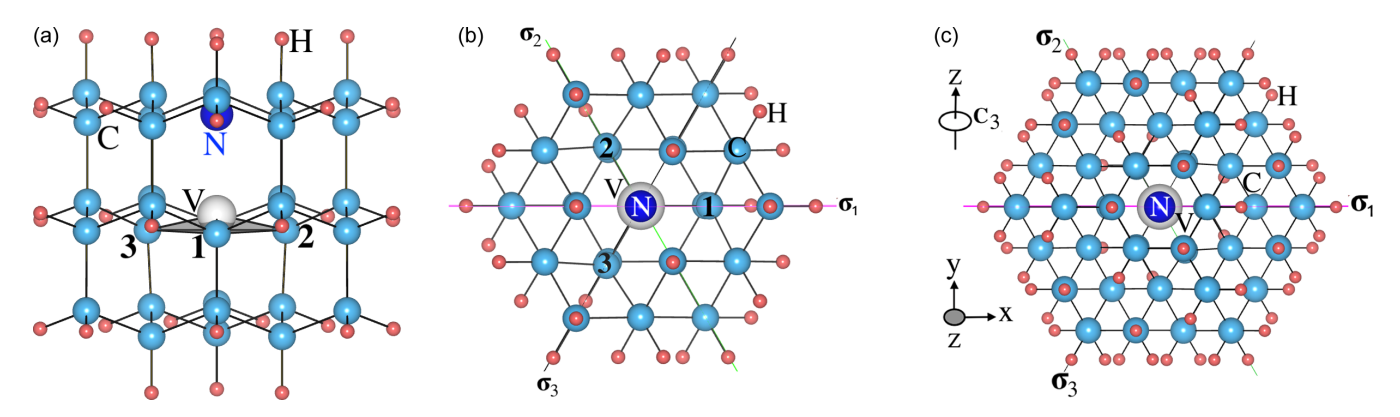


FIG. 1. (a) Side view and (b) top view of the NV⁻ center defect in a 70-atom diamond cluster with C_{3v} symmetry. (c) Top view of the NV⁻ center defect in a 162-atom cluster with C_{3v} symmetry. The color scheme is as follows: carbon (cyan), nitrogen (blue), vacancy (gray), hydrogen (pink). Carbon, nitrogen, vacancy, and hydrogen are denoted by C, N, V, and H, respectively. The rotation axis of the threefold symmetry (C_3) and the coordinate axes are shown. Here σ_1 , σ_2 , and σ_3 indicate vertical mirror planes passing through the carbons nearest to the vacancy with broken dangling bonds (labeled by 1, 2, and 3), the vacancy, and the z axis.

In order to remedy this limitation, quantum chemistry calculations [38,40,41] were performed for the NV⁻ center defect in diamond clusters, but the electronic structure of the defect states is not all consistent with experimental data [35,36,42]. For example, the ordering of the excited triplet and singlet states and the energy differences between the singlet states (or the excited triplet and singlet states) does not agree with experiment. As a middle ground, beyond-DFT ab initio results were combined with model Hamiltonians within manybody (perturbation) theory [19,25,43,44], finding agreement with experimental data [35–37,42]. However, Refs. [25,43,44] used fitting of the ab initio results to the model Hamiltonian parameters. More importantly, within these efforts [19,25,43,44], accounting for the effects of SOC and SSC is not straightforward. So far, zero-field splitting values induced by SOC and/or SSC have not been studied within many-body ab initio methods.

In this work, we investigate the electronic structure and magnetic properties of an NV⁻ center in diamond by systematically applying multiconfigurational quantum chemistry methods (beyond DFT) to hydrogen-passivated diamond clusters containing the defect. The critical ingredient for success in quantum chemistry calculations is to include several defectlocalized unoccupied states beyond dangling bond states, which differentiates our case from the previous quantum chemistry calculations [38,40,41]. By considering full electron correlation among these extra defect states and the dangling bond states, we determine excitation energies between the ground state and the excited spin-triplet and spin-singlet states as well as the character of the states. Furthermore, using the quantum chemistry methods, we examine effects of SOC and SSC on the spin-triplet states and identify characteristics of the split levels as well as the zero-field splitting values. This work is a quantum chemistry calculation of the zero-field splitting by SOC and SSC for an NV⁻ center in diamond. Our calculated results of the electronic structure and zero-field splitting are compared to recent experimental data with which we find agreement ranging from good to excellent.

This paper is structured as follows. In Sec. II we provide a brief overview of the NV⁻ center in diamond. In Sec. III we describe the structures of the clusters that are considered.

In Sec. IV we discuss our procedure of applying the quantum chemistry methods to the diamond clusters, while the technical detail with a flowchart is provided in the Appendix. In Sec. V we present our results of the energy separations and characteristics of the triplet and singlet states as well as the zero-field splitting in comparison to other theoretical studies and experimental data. In Sec. VI we provide our conclusion and outlook.

II. OVERVIEW OF NV- CENTER DEFECT

The deep NV⁻ center defect in diamond consists of a nitrogen atom substituting for carbon and a vacancy at its neighboring carbon site, as shown in Fig. 1(a). The axis connecting the vacancy and nitrogen sites is chosen to be the z axis. The defect has a C_{3v} point-group symmetry comprising two threefold rotational symmetries (C_3) about the z axis and three vertical mirror planes σ_i (i = 1, 2, 3) each passing through the nitrogen and nearest carbon atoms in the xy plane (Fig. 1).

For an NV⁻ center in diamond, experimental zero-phonon absorption spectra showed that the ground state is a spin-triplet ${}^{3}A_{2}$ state with an excitation energy of 1.945 eV to the first-excited spin-triplet ${}^{3}E$ [42] and that the excitation energy between the lowest and first-excited spin-singlet states (${}^{1}E^{-1}A_{1}$) is 1.190 eV [31]. Recent experimental data [35,36] showed that the singlet ${}^{1}A_{1}$ state has a higher energy than the singlet ${}^{1}E$ state. So far, there have been no direct measurements on the excitation energy of the spin-singlet ${}^{1}E$ state relative to the ground ${}^{3}A_{2}$ state. This excitation energy, however, can be deduced from the experimental energy difference between the ${}^{3}E$ and ${}^{1}A_{1}$ states (which is in the range of 0.321 to 0.414 eV [36,37]) as well as from the ${}^{1}A_{1}$ – ${}^{1}E$ energy difference.

III. CLUSTER STRUCTURES

To study the NV⁻ center in diamond, we consider two vacancy-centered clusters with hydrogen passivation, $C_{33}H_{36}N^-$ (70-atom cluster) and $C_{85}H_{76}N^-$ (162-atom cluster), which are created such that they have the correct $C_{3\nu}$ symmetry. The geometries of the clusters are constructed from

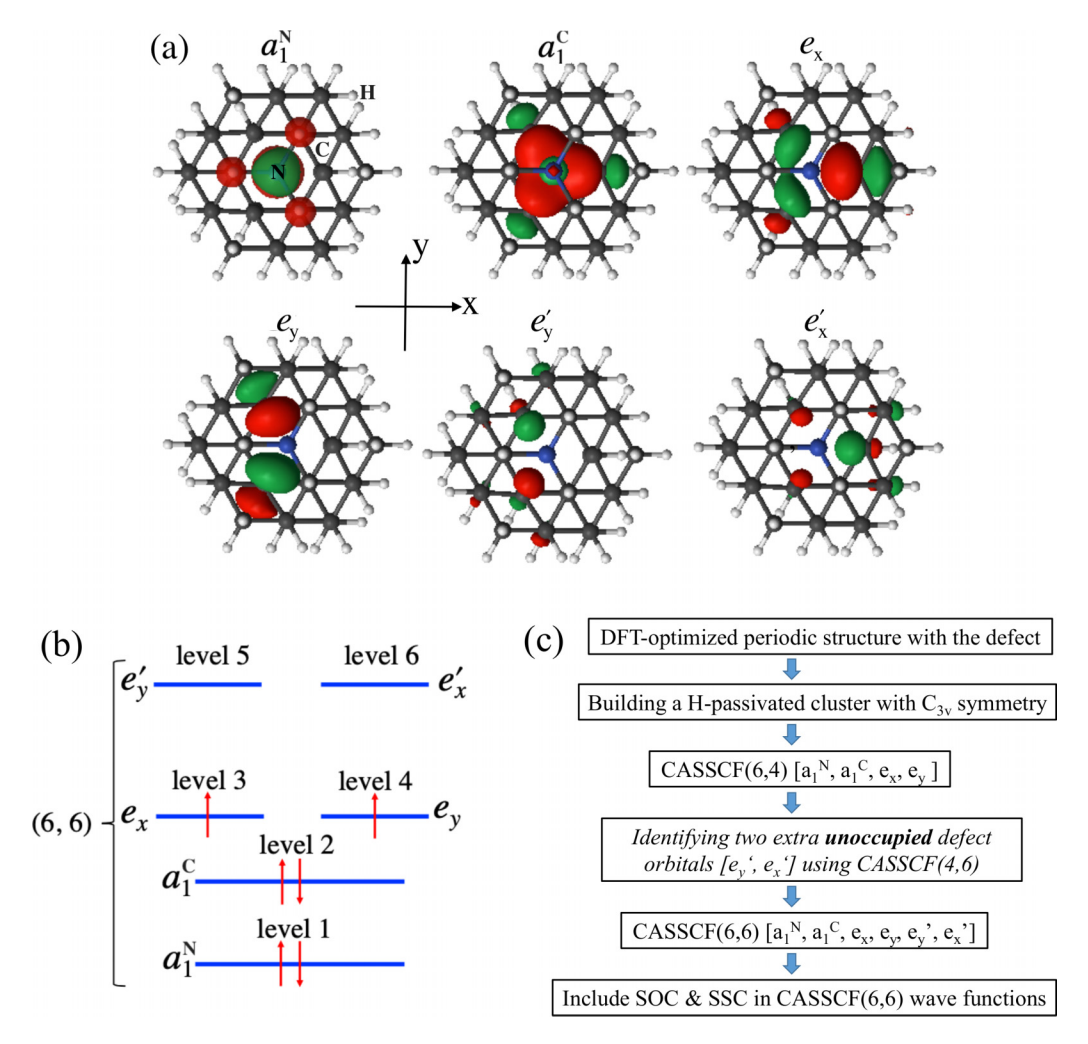


FIG. 2. (a) Top view of six defect orbitals (belonging to two A_1 and four E IRRep) in the active space with an isosurface value of 0.06 for the CASSCF(6,6) calculation of the 70-atom cluster. The similar six active orbitals are identified for the 162-atom cluster. The LUSCUS program [56] is used for visualization. (b) Nominal distribution of six electrons over the six active orbitals in the ground spin-triplet (${}^{3}A_{2}$) state. The actual occupation numbers of the a_{1}^{N} , a_{1}^{C} , e_{x} , e_{y} , e_{x}^{\prime} , e_{y}^{\prime} , are found to be 1.9986, 1.3753, 0.9883, 0.9883, 0.3248, and 0.3248, respectively, from the CASSCF(6,6) calculation. (c) Schematic flowchart of our computational procedure in which the italicized step is discussed in detail in the Appendix.

the DFT-optimized, C_{3v} -symmetric structure of a 215-atom cubic supercell with an NV⁻ center. The DFT calculation of the relaxation is performed for the cubic supercell with $4 \times 4 \times 4$ points within the Perdew-Burke-Ernzerhof (PBE) [45] generalized gradient approximation using QUANTUM ESPRESSO [46]. Ultrasoft pseudopotentials with scalar relativistic terms and nonlocal core corrections are used until the maximum residual force is less than 0.005 eV/Å. Figure 1 shows side and top views of the 70-atom cluster and a top view of the 162-atom cluster where the z axis is along the body-diagonal [111] direction in the cubic supercell. After the geometry optimization, the C_{3v} point-group symmetry is retained at the NV⁻ center in the supercell. For the DFToptimized supercell, the bond length between the nitrogen atom and the carbon atoms nearest to the vacancy is 2.734 Å, and the bond lengths between two nearest neighboring carbon atoms closest to the vacancy is 2.676 Å. These bond lengths agree well with the corresponding bond lengths reported from other DFT calculations [47]. The shortest distance between the vacancy and carbon (nitrogen) is 1.647 (1.690) Å. For

the clusters, the bond length between hydrogen and carbon is set to a standard value, 1.09 Å, and no further relaxation is carried out.

IV. QUANTUM CHEMISTRY METHODS

The quantum chemistry calculations are carried out in two steps: (i) complete active space self-consistent field (CASSCF) calculations with state average [48]; (ii) inclusion of SOC and SSC. We use both the OPENMOLCAS [49] code and the ORCA [50,51] code. The scalar relativistic effects are included based on the Douglas-Kroll-Hess Hamiltonian using relativistically contracted all-electron correlation-consistent polarized double-zeta basis sets, cc-pVDZ-DK [52,53], for all atoms in the clusters. A schematic flow chart of our computational procedure is shown in Fig. 2(c).

A. CASSCF calculations

In the CASSCF formalism [48], a many-body wave function is described as a linear combination of multiple Slater's

determinants, each of which is made of single-electron molecular orbitals. The coefficients of the Slater's determinants are referred to as configuration interaction (CI) expansion coefficients. A CASSCF wave function is partitioned into parts from inactive orbitals with double occupancy, virtual orbitals with zero occupancy, and active orbitals with occupancy between zero and two (i.e., 0, 1, or 2). In a CASSCF calculation, for a given spin multiplicity, any possible electron configurations or correlation within the active orbital space are included, while keeping the occupancies of the inactive and virtual orbitals fixed. However, electron excitation or correlations outside the active space are not included. Both the CI coefficients and the molecular orbitals are optimized through self-consistent calculations. Therefore, the choice of the active orbitals is critical for accurate CASSCF calculations. It was shown that the accuracy of CASSCF calculations is greatly improved by including extra molecular orbitals beyond frontier orbitals in the active space [48]. CASSCF wave functions are described in terms of spin-free basis states that correspond to all possible configurations generating the maximum M_z values, where M_z is an eigenvalue of the S_z operator (i.e., the z component of the total spin S). The state average is a technique to facilitate convergence of the excited-state CASSCF wave functions [48].

In order to determine the number and character of orbitals to be included in the active space, we start with a qualitative analysis of the electronic structure of an NVcenter from a single-electron point of view. The NV⁻ center in diamond has four broken dangling bonds, as shown in Fig. 1(a): three dangling bonds of the nearest neighboring carbon atoms to the vacancy $(d_1, d_2, and d_3)$, and the dangling bond of the nitrogen atom to the vacancy (d_N) . They form four single-electron molecular orbitals such as $a_1^C =$ $(d_1 + d_2 + d_3)/3$, $a_1^N = d_N$, $e_x = (2d_1 - d_2 - d_3)$, and $e_y =$ $(d_2 - d_3)/\sqrt{2}$ [29,54,55]. The first two orbitals transform as a function of the A_1 irreducible representation (IRRep), and the other two orbitals transform as functions of the E IRRep under the C_{3v} point group. It is known that the a_1^N orbital is deeply buried under the valence band of the diamond lattice, whereas the other three orbitals are within the band gap [28,29,54,55]. These three states are also referred to as in-gap defect states [19]. Now let us count the total number of electrons in the system. A carbon vacancy within diamond leaves four electrons in four dangling bonds. One of these carbon atoms is substituted with a nitrogen atom that has an extra electron (as compared to a carbon atom). The defect further acquires an additional electron and becomes negatively charged, resulting in a total number of six electrons that fill the defect states in accordance with the Hund's rules. In the spin-triplet ground state, the nominal occupancy is as follows: The defect state, a_1^N , which lies in the valence band, is doubly occupied, while the remainder of the four electrons are distributed amongst the in-gap states, with a_1^C being doubly occupied, and the degenerate orbitals $(e_x e_y)$ being singly occupied.

Inspired by the single-electron picture, we initially perform CASSCF calculations using the minimal active space consisting of six electrons and the four dangling bond orbitals $(a_1^N, a_1^C, e_x, \text{ and } e_y)$ for the 70-atom and 162-atom diamond clusters with C_{3v} symmetry, shown in Figs. 2(a) and 2(b). These calculations are referred to as CASSCF(6,4) following

the number of electrons and orbitals used in the active space. The excited-state wave functions obtained via CASSCF(6,4) calculations are found to be inconsistent with physical and chemical intuitions, and the corresponding excitation energies are highly overestimated compared to experiment. It is important to carry out CASSCF calculations beyond the minimal active space in order to include dynamic correlation. As a result, we expand the active space by including extra unoccupied defect-localized states. Note that the important criterion of extra unoccupied active orbitals in our case is orbital localization near the vacancy, whereas the active space is typically expanded based on an energy criterion only. The most common practice is to identify these extra states in the virtual space of the converged CASSCF(6,4) result. However, no such defect orbitals are found in the virtual space. Therefore, we introduce a series of CASSCF calculations discussed in the Appendix (Fig. 6) in order to identify and include extra defect orbitals in the active space. With this systematic CASSCF procedure, we find two unoccupied defect orbitals with E IRRep. In order to distinguish them from the dangling bond orbitals, e_x and e_y , they are, henceforth, referred to as e'_x and e'_{v} [Figs. 2(a) and 2(b)]. The inclusion of the second pair of E orbitals $(e'_x \text{ and } e'_y)$ in the active space is important for an accurate description of many-body correlations between electrons localized near the vacancy. Such an effect is not uncommon in quantum chemistry calculations for systems with highly populated localized orbitals. A canonical example is the double d-shell effect [57-60] in systems with late 3d transition metal atoms (e.g., Ni). In this case, a second set of 3d orbitals (referred to as 3d' orbitals) must be included in the active space (so that there are altogether 10 3d orbitals in the active space) for accurate energy calculations [57–60]. For the NV⁻ center, we have a similar situation with defect-localized orbitals occupied by a large number of electrons. This leads to strong dynamical correlations that need to be taken into account by including extra active orbitals $(e'_{x} \text{ and } e'_{y})$ in addition to the normal dangling-bond orbitals expected from the single-particle picture. With these two extra unoccupied orbitals, as well as the four dangling bond orbitals, we form an active space consisting of six electrons and six orbitals, and carry out CASSCF(6,6) calculations for both the total spin S = 1 and S = 0. Furthermore, in order to achieve high accuracy and exact numerical degeneracy (up to ~10 neV) in states with E symmetry, we carefully maintain the IRRep symmetry of all of the molecular orbitals and remove the surface-dominant orbitals in the self-consistent calculations.

B. Spin-orbit coupling and spin-spin coupling

For the ground ${}^{3}A_{2}$ state, the first-order SOC effect on the zero-field splitting vanishes and higher-order terms are negligibly small due to weak SOC. However, for the first-excited ${}^{3}E$ state, the first-order SOC effect becomes important within the subspace of degenerate states and the SOC-induced splitting turns out to be non-negligible. Therefore, for the most accurate calculation of SOC-induced splitting, we need to describe degenerate states the most accurately. In order to achieve this, state average is carried out only over the first-excited triplet pair (${}^{3}E$) of the CASSCF(6,6) wave functions. Then SOC is included in the converged CASSCF(6,6) spin-triplet wave functions within the atomic

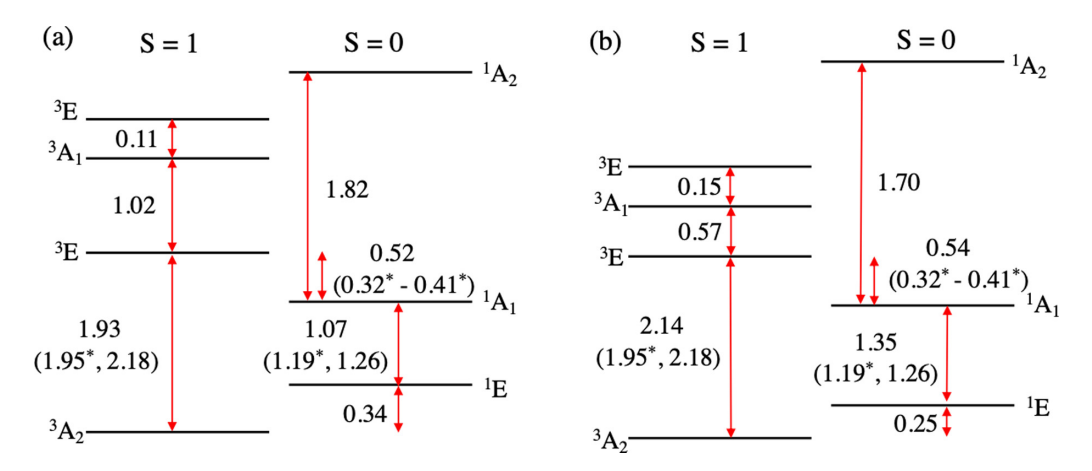


FIG. 3. Schematic level diagrams of the spin-triplet and spin-singlet states for (a) the 70-atom and (b) the 162-atom diamond clusters obtained using the quantum-chemistry method without SOC or SSC. Here full electron correlation within the six molecular orbitals [Figs. 2(a) and 2(b)] are considered. The experimental values [31,35–37,42] are shown inside parentheses. The experimental zero-phonon absorption energies are marked with *. All energy values are given in units of eV.

mean-field approximation [61], using the restricted active space state interaction (RASSI) method [62] implemented in OPENMOLCAS. For the CASSCF(6,6) energy eigenvalues and the SOC-induced zero-field splitting, OPENMOLCAS is used because it provides more accurate results due to purely symmetric orbitals and removal of surface-dominated orbitals (see the Appendix).

The zero-field splitting by the SSC is expected for all spintriplet states. This feature is computed for the CASSCF(6,6) wave functions using ORCA because it is not available in OPENMOLCAS. The SSC is calculated as the two-electron direct SSC over the CASSCF(6,6) wave functions using first-order perturbation theory [63], as implemented in ORCA. The CASSCF(6,6) wave functions using ORCA are obtained by following the CASSCF procedure sketched in the Appendix without orbital symmetrization, SUPERSYMMETRY keyword, and removal of surface orbitals, because they are not available in ORCA. We confirm that the zero-field splitting induced by SSC is not sensitive to technical details of the calculations (i.e., the cluster size, the size of the active space, and the number of roots included in the state average).

V. RESULTS AND DISCUSSION

A. Excitation energies

Figure 3 shows schematic level diagrams of our calculated spin-triplet and spin-singlet states for the two cluster sizes using OPENMOLCAS [quantum-chemistry methods, CASSCF(6,6)]. Note that we use the ground-state geometry without phonon modes and that we do not consider structural relaxation of the electronic excited states. An experimental absorption spectrum of an NV⁻ center in diamond consists of a sharp zero-phonon line with a broad spectrum of phonon side bands with several peaks [35,42]. With significant electron-phonon coupling, a zero-phonon absorption energy can noticeably differ from a vertical excitation energy. The latter energy is always higher than the former energy. The latter energy is commonly experimentally obtained from the maximum-intensity peak of the broad phonon side-band spectrum. The broadness of the phonon side bands provides some

uncertainty in the maximum-intensity peak energy, which renders uncertainty in the experimental vertical excitation energy. For comparison to experiment, we provide both experimental zero-phonon absorption energies and experimental vertical excitation energies in Fig. 3.

Our calculations show that the first-excited spin-triplet ${}^{3}E$ state is separated from the ground state $(^{3}A_{2})$ by 1.93 and 2.14 eV for the 70-atom and 162-atom clusters, respectively. This energy separation does not depend much on the cluster size and it is close to the experimental energies of zero-phonon absorption, 1.945 eV, and of vertical excitation, 2.18 eV [42]. We find that the lowest-energy singlet state has a character of ${}^{1}E$ and that the first-excited singlet ${}^{1}A_{1}$ state is located at 1.07 eV and 1.35 eV above the ${}^{1}E$ state for the 70-atom and 162-atom clusters, respectively. The ordering and the character of the singlet states agree with experiment, considering the experimental energies of zero-phonon absorption, 1.190 eV [31], and of vertical excitation, 1.26 eV [35]. Our results also reveal the energy differences between the triplet and singlet states. The ${}^{1}E$ state lies at 0.34 eV and 0.25 eV above the ${}^{3}A_{2}$ state for the 70-atom and 162-atom clusters, respectively. As a result, the energy gap between the ${}^{3}E$ and ${}^{1}A_{1}$ states becomes 0.52 and 0.54 eV for the 70-atom and 162-atom clusters, respectively. Although the energy gap between the ${}^{3}A_{2}$ state and the ${}^{1}E$ state has not been directly experimentally measured, the separation between the ${}^{3}E$ state and the ${}^{1}A_{1}$ state was measured to be 0.321-0.414 eV [36,37], which is in good agreement with our results. The second-excited (third-excited) triplet state has characteristics of ${}^{3}A_{1}$ (${}^{3}E$). The second-excited singlet ${}^{1}A_{2}$ state appears even above the thirdexcited triplet ${}^{3}E$ state. There are no experimental reports on the higher-energy levels or separations.

Our calculated results show that for the four lowest states $({}^{3}A_{2}, {}^{3}E, {}^{1}E, \text{ and } {}^{1}A_{1})$ the energy eigenvalues do not depend much on the cluster size, and that the small cluster-size dependence arises from two types of the finite-size effects such as shifts of one-electron levels and description of many-body correlations. Although we cannot separate the two effects, the comparison between the energies of the smaller active space and the CAS(6,6) suggests that dynamic correlations

TABLE I. Our calculated excitation energies with respect to the ground state $(^{3}A_{2})$ in units of eV for the two cluster sizes using the quantum chemistry method (without SOC or SSC), in comparison to previous theoretical studies and experimental data. For our calculations, neither the relaxation energy of the excited states nor vibration energies are included. In other words, we use the same geometry for the ground state and all excited triplet and singlet states. Zero-phonon absorption energies are marked with *. The unmarked experimental value correspond to the vertical excitation energy, i.e., the maximum-intensity peak energy of the phonon side band spectra [42]. The experimental energy of the ^{1}E state relative to the ground-state energy is converted from the following two measurements: (a) the zero-phonon absorption energy between the ^{1}E and $^{1}A_{1}$ states which is 1.190 eV [31]; (b) the energy difference between the $^{1}A_{1}$ and ^{3}E states which is 0.321–0.414 eV [36,37].

Reference\Electronic state	^{3}E	${}^{3}A_{1}$	^{3}E	^{1}E	$^{1}A_{1}$	${}^{1}A_{2}$
Experiment [31,35–37,42]	1.945*[42]			0.34*-0.43*	1.51*-1.60*	
	$\sim 2.18 [42]$			[36,37]	[31]	
C ₃₃ H ₃₆ N ⁻ CASSCF(6,6)	1.93	2.95	3.06	0.34	1.41	3.23
(This work)						
C ₈₅ H ₇₆ N ⁻ CASSCF(6,6)	2.14	2.71	2.86	0.25	1.60	3.30
(This work)						
C ₃₃ H ₃₆ N ⁻ CASSCF(6,8) [41]	2.48					
C ₄₉ H ₅₂ N ⁻ CASSCF(6,8) [41]	2.57					
C ₁₉ H ₂₈ N ⁻ CASSCF(8,11) [40]	0.98		1.22	0.44	1.00	$1.13(^{1}E)$
C ₁₉ H ₂₈ N ⁻ MRCI(8,10) [40]	1.36		1.61	0.50	1.23	$1.37(^{1}E)$
C ₄₂ H ₄₂ N ⁻ MCCI [38]	1.96, 1.93			0.63, 0.64	2.06	
GW + BSE [43]	2.32			0.40	0.99	$2.25(^{1}E')$
GW fit to model [44]	2.0*			\sim 0.5	~1.5	$\sim 3.0(^{1}E')$
	2.1					
CI-CRPA [19]	1.75*			0.49	1.41	$3.09(^{1}E')$
(512-atom supercell)	2.02					
Beyond-RPA [25] with	2.00			0.56	1.76	
quantum embedding theory						
C ₃₃ H ₃₆ N ⁻ DFT [39]	1.77*			0.44	1.67	
DFT (512-atom	1.71*			0.9	0.0, 2.2	
supercell) [28]	1.91					
C ₄₂ H ₄₂ N ⁻ DFT [38]	1.27			0.42	2.10	
					$1.26(^{1}A')$	
C ₂₈₄ H ₁₄₄ N ⁻ DFT [38]	1.90			0.48	2.03	
					$1.26(^{1}A')$	

contribute more to the cluster-size dependence. We find that the cluster-size dependence becomes more apparent for higher-energy states, especially for the second- and third-excited triplet states (3A_1 and 3E). Depending on the cluster size, the energy separations change but the ordering of the states does not change. A similar trend of the cluster-size dependence was reported in the complete-active space approach, using DFT Kohn-Sham orbitals and density-matrix renormalization group [64]. This trend can be understood by the fact that higher-energy levels have stronger electron correlations which requires inclusion of more empty orbitals in the active space. Since experimental data are available for mainly up to the first-excited triplet 3E state, we do not further study an effect of cluster size on the electronic structure.

B. Comparison to other ab initio studies

Let us now compare our calculated energies of the spintriplet and spin-singlet states (${}^{3}A_{2}$, ${}^{3}E$, ${}^{1}E$, and ${}^{1}A_{1}$) to the previous *ab initio* theoretical studies. See Table I and Fig. 4. In our analysis, we focus on the four lowest states because only the level separations among them were experimentally measured and because higher-energy states are more sensitive to the cluster size and the size of the active space. (For example, the higher-energy ${}^{1}E'$ state that many-body theory studies predicted [19,43,44] has not been observed [35].) We first discuss comparison to other DFT calculations and then to other quantum-chemistry studies as well as many-body theory studies, separately.

Earlier DFT studies of an NV $^-$ center in diamond clusters and periodic supercells [28,38,39,41,65,66] showed that the calculated excitation energy of the 3E state more or less agrees with our result and experiment except for Ref. [38]. However, DFT-calculated energies of the singlet states are scattered in a wide range and the ordering of the triplet and singlet states is inconsistent with recent experiment. This trend is understandable considering that DFT poorly describes the singlet states due to the lack of multiconfigurational and multireference nature.

In the previous quantum-chemistry studies of an NV⁻ center in diamond clusters [38,40,41], either the excitation energies are significantly different from experiment, or the ordering of the singlet and triplet states is reversed. More specifically, CASSCF(6,8) calculations discussed in Ref. [41] showed that the excitation energy of the ³E state is 0.5–0.6 eV (0.3–0.4 eV) higher than our result (experiment). The singlet states were not investigated in that work. In the CASSCF(8,11) calculations presented in Ref. [40], the excitation energy of the ³E state is about 1.0 eV lower than our result or experiment, and the singlet ¹A₁ state is slightly above

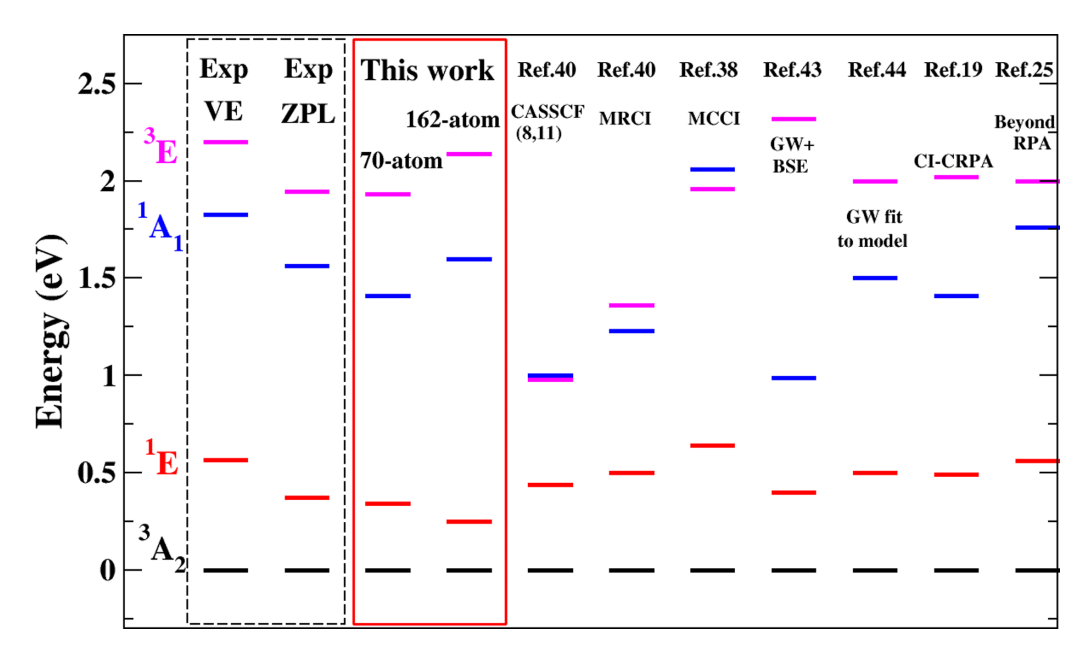


FIG. 4. Comparison of our calculated spin-triplet and spin-singlet energies to the previous many-body theoretical studies [19,25,38,40,43,44] as well as the experimental zero-phonon lines (ZPL) and vertical excitations (VE) [31,35–37,42]. The experimental VE are energies of the maximum-intensity peak of the broad phonon side-band absorption spectra. The experimental ZPL and VE energies of the ^{1}E and $^{1}A_{1}$ states (relative to the ground state) are taken from the midpoint of the experimental range [36] of the separation between the ^{3}E and $^{1}A_{1}$ states, while keeping the $^{1}A_{1}$ – ^{1}E energy difference fixed as the experimental value of 1.190 eV [31].

the triplet ${}^{3}E$ state, which does not agree with our result or recent experiment. This discrepancy arises from the following two major differences. Firstly, the geometries of our clusters (70-atom and 162-atom) are obtained from the DFT-optimized geometry of bulk 215-atom supercell with an NV center, while the geometry of the 48-atom cluster in Ref. [40] was obtained from the geometry optimization of the finite cluster using CASSCF, where the C_{3v} symmetry was broken. Secondly, we consider six orbitals localized near the vacancy with six electrons in the active space, whereas Ref. [40] selected 11 orbitals (not shown in the reference) and eight electrons in the active space for the 48-atom cluster from orbital studies of a 16-atom cluster. Their multireference configuration interaction (MRCI) calculations [40] somewhat increase the energies of the triplet and singlet states with the correct ordering of the excited triplet and singlet states. However, the energy of the ${}^{3}E$ state remains lower than our value by about 0.6 eV. Monte Carlo configuration interaction (MCCI) studies [38] showed the energy of the ${}^{3}E$ state in agreement with our result and experiment. However, the ordering of the 3E and ${}^{1}A_{1}$ states is reversed. See Table I and Fig. 4. In the MCCI studies [38], a 85-atom cluster with the DFT-optimized geometry was used with orbitals which are not necessarily localized near the vacancy. The discrepancies between our results and all of the earlier quantum-chemistry calculations mostly arise from the choice of orbitals in the active space. One of the most common ways to choose active orbitals is to use single-electron molecular orbitals in the vicinity of the band gap such as orbitals near the highest occupied molecular orbitals (HOMO) and lowest unoccupied molecular orbitals (LUMO). For a hydrogen-passivated diamond cluster with an NV⁻ center, either this common practice within CASSCF or MRCI, or an automatic choice of the active space in MCCI,

may result in nonphysical surface-dominated orbitals in the CI basis set. As shown in Fig. 2(a), in our case, all six orbitals in the active are localized near the vacancy defect.

An earlier many-body perturbation study [43] based on the GW approximation with Bethe-Salpeter equation (BSE) provided the singlet-singlet $({}^{1}A_{1}-{}^{1}E)$ energy difference about 0.6 eV lower than our result and recent experiment [35,36], although the energy of the ${}^{1}E$ state relative to the ground state, as well as the ordering of the two singlet states are in agreement with the recent experimental data. On the other hand, recent many-body studies [19,25,44] showed more promising results by using effective many-body model Hamiltonians with parameters obtained from (or fitted to) ab initio calculations in order to properly include many-body character in the wave functions. For example, additional unoccupied defect states (resonant to the conduction band) and doubly occupied defect states (in the valence band) were included in the configuration interaction constrained random phase approximation (CI-CRPA) method [19]. This is analogous to our inclusion of unoccupied level 5 and 6 and doubly occupied level 1 [Fig. 2(b)] in the active space for proper treatment of electron correlation. Their results are closest to our result among the previous studies that we have discussed (see Fig. 4 and Table I). Yet, there are some differences. In the fitting of GW-calculated bands to the model Hamiltonian [44] (in the CI-CRPA method [19]), the singlet-singlet energy difference is about 0.2-0.3 eV (0.3-0.4 eV) lower than our result and experiment. In the beyond-RPA implemented in the quantum embedding theory [25], the energy difference between the ${}^{3}E$ and ${}^{1}A_{1}$ states is somewhat smaller than our result and experiment. This discrepancy may arise from missing orbital configurations in the ${}^{1}E$ and ${}^{1}A_{1}$ states in Refs. [19,25,44] that are discussed in Sec. VC. Here we stress that it does

TABLE II. Characteristics of the calculated energy eigenstates for the 70-atom cluster using the configuration (spin-free) basis states. Here the configuration basis states are all possible states generating the maximum M_z value from the six active orbitals (Fig. 2) for a given total spin S, where M_z is an eigenvalue of S_z . Each box represents an orbital. Up and down arrows denote spin-up and spin-down electrons. Each configuration represents a Slater's determinant of the orbitals with 2S + 1 degeneracy. Percentages denote orbital configuration weights. Only configurations with weights greater than 5% or above are listed. Weights greater than 10% are denoted as boldface.

State	Configuration (weight) $a_1^N a_1^C e_x e_y e_y' e_x'$
$^3A_2(\Psi_{1,T})$	$\uparrow\downarrow\uparrow\downarrow\uparrow$ \uparrow \downarrow
$^{3}E\left(\Psi_{2,T}\right)$	
$(\Psi_{3,T})$	$\uparrow\downarrow\uparrow\uparrow\uparrow\downarrow\downarrow \qquad (\mathbf{38\%}), \qquad \uparrow\downarrow\uparrow\uparrow\uparrow\downarrow\uparrow \qquad (\mathbf{30\%}), \qquad \uparrow\downarrow\downarrow\uparrow\uparrow\uparrow\uparrow\downarrow\downarrow \qquad (\mathbf{7\%}), \qquad \uparrow\downarrow\downarrow\uparrow\uparrow\uparrow\uparrow\downarrow\downarrow \qquad (\mathbf{5\%})$
$^3A_1(\Psi_{4,T})$	$ \uparrow\downarrow\uparrow\uparrow\downarrow\uparrow \qquad \uparrow \qquad (\mathbf{29\%}), \qquad \uparrow\downarrow\downarrow\uparrow\downarrow \qquad \uparrow \qquad \uparrow \qquad (\mathbf{29\%}), \qquad \uparrow\downarrow\downarrow\uparrow\uparrow\downarrow\downarrow \qquad \uparrow \qquad (9\%), \qquad \uparrow\downarrow\downarrow\uparrow\uparrow\downarrow\downarrow \qquad \uparrow \qquad (6\%), \qquad \uparrow\downarrow\downarrow\uparrow\uparrow\downarrow\uparrow\uparrow \qquad (6\%), $
$^{3}E\left(\Psi_{5,T}\right)$	
$(\Psi_{6,T})$	
$^{1}E\left(\Psi_{1,S}\right)$	
$\left(\Psi_{2,S}\right)$	
$^1A_1(\Psi_{3,S})$	
$^1A_2(\Psi_{4,S})$	

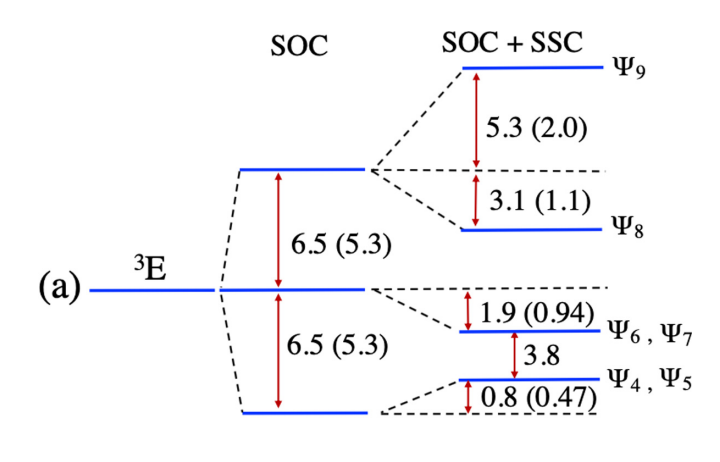
not seem to be straightforward to include effects of SOC and SSC within the formalisms used in Refs. [19,25,44] in contrast to the quantum chemistry methods where such effects can be added to the many-body wave functions without an introduction of new fitting parameters (see Sec. V D).

C. Characteristics of energy eigenstates

We now discuss characteristics of our calculated triplet and singlet energy eigenstates (Table II). Here we use configuration basis states which are all possible states generating the maximum M_z value from the six active orbitals for a given total spin S, where M_z is an eigenvalue of the S_z operator. The total wave functions in terms of true S_z eigenstates are obtained when SOC is applied to the many-body (CASSCF) wave functions within the RASSI method [62] using the Wigner-Eckart theorem. The SOC effect is discussed later in Sec. V D.

for the notations. The former states indicate single excitations from the doubly occupied a_1^C level, while the latter state indicates a double excitation from the a_1^C level. These configurations have not been considered in Refs. [25,44,54,55,67]. Although the dominant configurations for the 1E and 1A_1 states listed in Table II agree with those shown in Ref. [19], our weights of the aforementioned single and double excitations are significantly larger than those in Ref. [19]. The inclusion of these excitations and their significant weights in our work may be the sources of the discrepancy between our result and those obtained in Refs. [19,25,44] and they may also affect the intersystem crossing.

Furthermore, above the first-excited triplet ${}^{3}E$ state and the first-excited ${}^{1}A_{1}$ state, we find the triplet ${}^{3}A_{1}$ and ${}^{3}E$ states and the singlet ${}^{1}A_{2}$ state. Due to the lack of experimental data beyond the four lowest states, we only briefly mention these higher-energy states. Our higher-energy states differ from those in the literature [19,40,43,44,54,55]. As shown in Table II, the main contributions to these states originate from single excitations from the a_1^C , e_x , or e_y orbital to beyond the dangling bond orbitals $(e'_x \text{ and } e'_y)$ [Fig. 2(b)]. On the other hand, the previous many-body and molecular-model studies [43,44,54,55] were mostly obtained considering only three or four dangling bond orbitals $(a_1^N, a_1^C, e_x, \text{ and } e_y)$. As discussed earlier, the higher-energy states are more sensitive to the size of active space and cluster size than the four lowest states due to stronger electron correlation. Note that the ${}^{1}E'$ state predicted in the literature has not been experimentally observed [35].



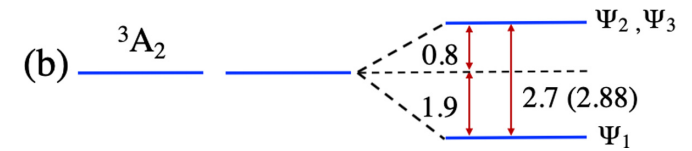


FIG. 5. Schematic diagram of our calculated energy level splitting of (a) the first-excited triplet 3E state and (b) the ground 3A_2 state due to SOC and SSC in units of GHz (for 70-atom cluster). The experimental values [68] are shown inside parentheses. States $\Psi_{1,\dots,9}$ are defined in Table IV.

D. Zero-field splitting

All of the spin-triplet states that we discussed earlier are split due to SOC and/or SSC. Note that SOC plays an important role in the zero-field splitting only for the degenerate levels in this system because of the weak SOC. Since experimental data do not exist for higher-energy states, we present calculated zero-field splitting values of the ground ${}^{3}A_{2}$ state and the first-excited triplet ${}^{3}E$ state only. Figure 5 and Table III show our calculated level splitting by SOC alone and by SOC in combination with SSC (SOC+SSC) for the ${}^{3}A_{2}$ and ${}^{3}E$ states, separately, compared to experimental data [68]. Table IV lists the corresponding eigenvectors $\Psi_{1,\dots,9}$ obtained from the quantum chemistry calculations including SOC and SSC. The SOC-induced level splitting is obtained for the 70-atom and 162-atom clusters, while the SSC-induced splitting is obtained for the 70-atom cluster. Regarding the

SOC+SSC induced splitting for the 162-atom cluster, we use the SSC-induced splitting for the 70-atom cluster since the SSC-induced splitting does not depend much on cluster size. Let us now discuss the ${}^{3}A_{2}$ and ${}^{3}E$ states separately.

The SOC does not split the 3A_2 state to the first order and its splitting by higher-order SOC is negligible. However, we find that the SSC splits the 3A_2 state into one lower nondegenerate level with $M_z = 0$ and one higher doubly degenerate level with $M_z = \pm 1$ by -1.9 GHz and 0.8 GHz, respectively. (See the eigenvectors $\Psi_{1,2,3}$ in Table IV.) Therefore, the energy separation between them is about 2.7 GHz, which is in excellent agreement with the experimental value of 2.88 GHz [68] as well as a previous DFT calculation [47].

On the other hand, the SOC splits the ${}^{3}E$ state into three (degenerate) groups, each of which has eigenvalues of the z component of orbital angular momentum L_7 of ± 0.46 (± 0.53) for the 70-atom (162-atom) cluster. The separation of the levels is about 6.5 GHz for the 70-atom cluster (Fig. 5) and about 8.1 GHz for the 162-atom cluster. Our calculated level splitting values show a weak cluster-size dependence and they are somewhat larger than the experimental value of 5.3 GHz [68]. A possible reason for this is the dynamic Jahn-Teller effect [69,70] and the resulting quenching of SOC (i.e., Ham reduction factor [37,71,72]). Note that our calculations are done for zero strain without electron-phonon coupling. Quantum-chemistry calculations of electron-phonon coupling and the dynamic Jahn-Teller effect are worth investigating in the future. In addition to the SOC-induced splitting, the SSC further shifts the lowest degenerate level upward by 0.8 GHz $(\Psi_4, \Psi_5 \text{ in Table IV})$ and moves the second degenerate level downward by 1.9 GHz (Ψ_6 , Ψ_7). In this case, the degeneracy still holds. Interestingly, the amount of the downward level shift is almost twice that of the upward shift. The trend of the level-shift direction as well as the ratio between the downward and upward shift amount are in good agreement with experiment [68], although our shifted values are off by a factor of 2 compared to experiment. We also find that the SSC splits the third doubly degenerate level into two separate levels (Ψ_8 , Ψ_9): one level shifts downward by 3.1 GHz and the other moves upward by 5.3 GHz. Again, the trend of the level shift agrees with experiment [68], although the calculated shift amount is greater than experiment by a factor of 2 or 3. This

TABLE III. Calculated SOC- and SSC-induced level splitting of the ground state $(^3A_2)$ and the first-excited triplet (^3E) state from the quantum chemistry method for the 70-atom and 162-atom clusters in comparison to experiment. The level splitting values for the 162-atom cluster are shown in the parentheses. All energies are expressed relative to the lowest SOC-included energy in each triplet state $(^3A_2$ or $^3E)$. One exception is the experimental zero-field splitting of the 3A_2 state marked by \dagger in which only the difference is known. The eigenvectors including SOC, $\Psi_{1,...,9}$, are defined in Table IV.

State		SOC (GHz) (Theory)	SSC (GHz) (Theory)	SOC+SSC (Theory, GHz)	SOC (GHz) (Expt.) [68]	SOC+SSC (Expt., GHz) [68]
$^{3}A_{2}$	Ψ_1	0	-1.9	-1.9	0	0^{\dagger}
	Ψ_2,Ψ_3	0	0.8	0.8	0	2.88^{\dagger}
^{3}E	Ψ_4,Ψ_5	0	0.8	0.8 (0.8)	0	0.47
	Ψ_6, Ψ_7	6.5 (8.1)	-1.9	4.6 (6.2)	5.3	4.36
	Ψ_8	13.0 (16.2)	-3.1	9.9 (13.1)	10.6	9.52
	Ψ_9	13.0 (16.2)	5.3	18.3 (21.5)	10.6	12.62

TABLE IV. Energy eigenvalues and eigenvectors corresponding to the ground- and first-excited triplet 3A_2 and 3E states for the 70-atom and 162-atom clusters calculated using the quantum chemistry methods including SOC and SSC. The energies are relative to the lowest SOC-included energy of each triplet state (3A_2 or 3E), as listed in Table III and shown in Fig. 5. The energy values in the parentheses are for the 162-atom cluster. Here $\Psi_{1,T}$, $\Psi_{2,T}$, and $\Psi_{3,T}$ are our calculated eigenstates (without SOC and SSC) listed in Table II.

State		Energy (GHz)	Total wave function
$^{3}A_{2}$	Ψ_1	-1.9 (-1.9)	$\Psi_{1,T} S = 1, M_z = 0 \rangle$
	Ψ_2	0.8 (0.8)	$\frac{1}{\sqrt{2}} \Psi_{1,T} (S=1, M_z=1\rangle + S=1, M_z=-1\rangle)$
	Ψ_3	0.8 (0.8)	$\frac{1}{\sqrt{2}}\Psi_{1,T} (- S=1, M_z=1\rangle + S=1, M_z=-1\rangle)$
^{3}E	Ψ_4	0.8 (0.8)	$\frac{1}{\sqrt{2}}(\Psi_{2,T} + i\Psi_{3,T}) S = 1, M_z = 1 \rangle$
	Ψ_5	0.8 (0.8)	$\frac{1}{\sqrt{2}}(\Psi_{2,T} - i\Psi_{3,T}) S = 1, M_z = -1 \rangle$
	Ψ_6	4.6 (6.2)	$\Psi_{2,T} \mid S=1, M_z=0 \rangle$
	Ψ_7	4.6 (6.2)	$\Psi_{3,T} S=1, M_z=0 \rangle$
	Ψ_8	9.9 (13.1)	$\frac{1}{2}\Psi_{2,T}(S=1,M_z=1\rangle+ S=1,M_z=-1\rangle)-i\frac{1}{2}\Psi_{3,T}(S=1,M_z=1\rangle- S=1,M_z=-1\rangle)$
	Ψ_9	18.3 (21.5)	$-\frac{1}{2}\Psi_{2,T}(S=1,M_z=1\rangle - S=1,M_z=-1\rangle) + i\frac{1}{2}\Psi_{3,T}(S=1,M_z=1\rangle + S=1,M_z=-1\rangle)$

overestimated SSC contribution may partially arise from our first-order perturbation treatment of SSC.

VI. CONCLUSION AND OUTLOOK

We have developed a systematic numerical procedure to compute the electronic structure and magnetic properties of an NV⁻ center defect in diamond clusters, using the (multiconfigurational) quantum chemistry methods, where electron correlation is properly included. We found that the crucial constituent in the procedure is to identify and include extra unoccupied defect orbitals (beyond the four dangling bond orbitals) in the active space. Our quantum chemistry calculations showed that the first-excited spin-triplet ${}^{3}E$ state is separated from the ground state $(^{3}A_{2})$ by 1.93–2.14 eV, while the first-excited spin-singlet ${}^{1}E$ state is separated from the lower-energy ${}^{1}A_{1}$ state by 1.07–1.35 eV. In addition, we found that the ${}^{3}E$ state is separated from the ${}^{1}A_{1}$ state by 0.52-0.54 eV. Our calculated triplet-triplet, singlet-singlet, and triplet-singlet excitation energies as well as the ordering of the triplet and singlet states are in good agreement with experiment. We found additional configurations which significantly contribute to the ${}^{1}E$ and ${}^{1}A_{1}$ states, which have not been considered before. Furthermore, SOC and SSC were included in our many-body wave functions, finding that the SSC splits the ${}^{3}A_{2}$ state by 2.7 GHz and that a combination of the SOC and SSC splits the ${}^{3}E$ state into two degenerate levels and two nondegenerate levels. The SSC-induced splitting of the ${}^{3}A_{2}$ state and the SOC-induced splitting of the ${}^{3}E$ state are in good agreement with experiment. When both SOC and SSC are included in the ${}^{3}E$ state, the calculated trend of the level splitting agree well with experiment and the splitting amount is mostly deviated from experiment by a factor of two.

The numerical procedure that we developed in this work can be applied to other deep defects in wide band-gap semiconducting materials such as group-IV defects and transition-metal defects in diamond or silicon carbide, or rare-earth defects in silicon or complex oxides, as long as a sufficient number of defect-localized orbitals is judiciously chosen for the active space while retaining the defect symmetries and orbital degeneracy as accurately as possible. This procedure may also be extended to obtain radiative transition

rates between the states and can be applied to deep defects with external perturbations such as electric fields and strains. Therefore, our findings open an avenue to be able to screen other defects desirable for specific applications beyond to accurately predict the properties of their excited states.

ACKNOWLEDGMENTS

The authors were supported by the National Science Foundation under a collaborative grant (Grants No. DMR-1737921 for S.E.E. and K.P. and No. DMR-1738076 for P.D.). We are grateful to Adam Gali, Kai-Mei Fu, Marcus Doherty, and Audrius Alkauskas for useful comments on the paper. The computational support was provided by the Virginia Tech Advanced Research Computing and the Extreme Science and Engineering Discovery Environment (XSEDE) under Project No. DMR060009N (K.P.) and Project No. PHY180014 (P.D.), which are supported by the National Science Foundation Grant No. ACI-1548562.

APPENDIX: PROCEDURE OF IDENTIFYING ACTIVE ORBITALS AND PERFORMING CASSCF(6,6)

In order to identify extra unoccupied defect orbitals beyond the four dangling bond orbitals as discussed in Sec. IV, we carry out the following systematic procedure for the 70-atom and 162-atom clusters with the total spin S = 1. Figure 6 summarizes the CASSCF procedure using OPEN-MOLCAS. Note that extra unoccupied defect orbitals cannot be found from the CASSCF(6,4) calculation. The doubly occupied a_1^N orbital is known to have a lower energy than the doubly occupied a_1^C orbital and the former is buried in the bulk valence band. Therefore, excluding the a_1^N orbital, we envision a CASSCF(4,6) calculation where six active orbitals consist of three dangling bond orbitals (a_1^C, e_x, e_y) , two unoccupied defect orbitals with E IRRep, and one unoccupied defect orbital with A_1 IRRep. Keeping this in mind, we first perform a CASSCF(4.6) calculation (with state average over six roots) using four active electrons and initial six active orbitals guessed by OPENMOLCAS. Then converged orbitals from the CASSCF(4,6) calculation are fully symmetrized with C_{3v} symmetry, using the LIBMSYM program [73] that is

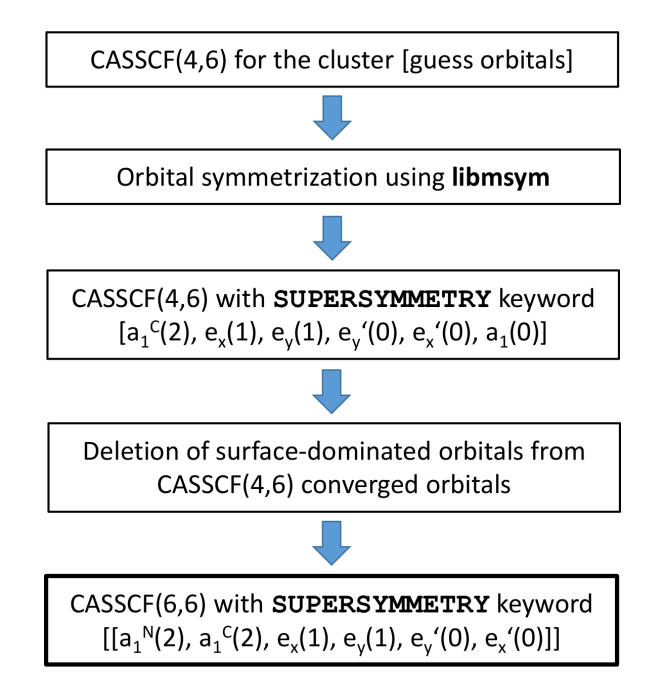


FIG. 6. Schematic diagram of our practical procedure to identify two extra unoccupied defect orbitals and to preform the CASSCF(6,6) calculations of an NV⁻ center defect in the hydrogen-passivated 70-atom and 162-atom diamond clusters, using OPEN-MOLCAS. Here initial orbitals in the active space are listed within brackets, where nominal occupation numbers for the spin-triplet ground state are shown inside parentheses. The nominal occupation numbers differ from the actual occupation numbers. The orbitals inside double brackets are final converged orbitals. LIBMSYSM is an orbital-symmetrization program [73] and the function of SUPERSYM-METRY keyword is defined in the text of the Appendix.

interfaced with OPENMOLCAS. The LIBMSYM program can deal with higher point-group symmetries than twofold symmetry. Now each molecular orbital in the inactive, active, and virtual spaces has its own pure IRRep symmetry. Among these symmetrized orbitals, we identify two extra unoccupied orbitals localized near the defect with e_x and e_y symmetries, as well as one unoccupied defect orbital with a_1 symmetry. In order to distinguish these extra orbitals with e_x and e_y symmetries from the singly occupied dangling bond orbitals (e_x and e_y),

the former orbitals are referred to as e'_x and e'_y orbitals. Now using these extra three unoccupied defect orbitals as well as the three dangling bond orbitals as initial six active orbitals, we carry out another CASSCF(4,6) calculation with restricted orbital rotations throughout iterations, in other words, orbital rotations (or optimization) are allowed only among the orbitals belonging to the same IRRep. This restriction can be achieved using SUPERSYMMETRY keyword in OPENMOL-CAS code. The steps of libmsym and SUPERSYMMETRY are crucial to maintain purely-symmetric orbitals throughout the self-consistent calculations and more importantly to retain the perfect degeneracy of the converged CASSCF energy eigenvalues (the accuracy of ~10 neV) belonging to the IRRep E. Such high accuracy is required for an accurate calculation of zero-field splitting induced by SOC. After the second CASSCF(4,6) calculation, the two unoccupied defect orbitals, e'_{r} and e'_{v} , remain in the active space.

In our molecular cluster models for an NV- center, the hydrogen-passivated surface is artificial since it does not exist in a diamond lattice. Therefore, orbitals localized at the surface are not associated with the defect in a diamond lattice. In order to reduce an effect of such surface-dominated orbitals on the orbital optimization, we remove several tens of surface-dominated orbitals near the active space from the converged orbitals in the second CASSCF(4,6) calculation. More surface orbitals are removed for a larger cluster. After this step, we now carry out a CASSCF(6,6) calculation with SUPERSYMMETRY keyword using the identified e'_r and e'_{v} orbitals [from the CASSCF(4,6) calculation] as well as the four dangling bond orbitals as initial active orbitals. We check that the energy levels (root energies) obtained from the CASSCF(6,6) calculation do not change as the number of removed surface orbitals varies, as long as enough number of surface orbitals are removed near the active space.

The similar procedure to Fig. 6 is carried out for the total spin S=0 with state average over six roots for both 70-atom and 162-atom clusters. Then we perform another CASSCF(6,6) calculation with state average over four roots, using the converged CASSCF(6,6) orbitals, in order to retain the perfect degeneracy of the CASSCF energy eigenvalues in the E IRRep and the localization of the active orbitals. We emphasize that the orbital symmetrization is more important for the spin-singlet states than for the spin-triplet states.

^[1] J. R. Maze, P. L. Stanwix, J. S. Hodges, S. Hong, J. M. Taylor, P. Cappellaro, L. Jiang, M. V. Gurudev Dutt, E. Togan, A. S. Zibrov, A. Yacoby, R. L. Walsworth, and M. D. Lukin, Nanoscale magnetic sensing with an individual electronic spin in diamond, Nature (London) 455, 644 (2008).

^[2] G. Balasubramanian, I. Y. Chan, R. Kolesov, M. Al-Hmoud, J. Tisler, C. Shin, C. Kim, A. Wojcik, P. R. Hemmer, A. Krueger, T. Hanke, A. Leitenstorfer, R. Bratschitsch, F. Jelezko, and J. Wrachtrup, Nanoscale imaging magnetometry with diamond spins under ambient conditions, Nature (London) 455, 648 (2008).

^[3] B. Hensen, H. Bernien, A. E. Dréau, A. Reiserer, N. Kalb, M. S. Blok, J. Ruitenberg, R. F. L. Vermeulen, R. N. Schouten, C.

Abellán, W. Amaya, V. Pruneri, M. W. Mitchell, M. Markham, D. J. Twitchen, D. Elkouss, S. Wehner, T. H. Taminiau, and R. Hanson, Loophole-free bell inequality violation using electron spins separated by 1.3 kilometres, Nature (London) **526**, 682 (2015).

^[4] T. H. Taminiau, J. Cramer, T. van der Sar, V. V. Dobrovitski, and R. Hanson, Universal control and error correction in multi-qubit spin registers in diamond, Nat. Nanotechnol. 9, 171 (2014).

^[5] G. Waldherr, Y. Wang, S. Zaiser, M. Jamali, T. Schulte-Herbrüggen, H. Abe, T. Ohshima, J. Isoya, J. F. Du, P. Neumann, and J. Wrachtrup, Quantum error correction in a solid-state hybrid spin register, Nature (London) 506, 204 (2014).

- [6] L. Robledo, L. Childress, H. Bernien, B. Hensen, P. F. A. Alkemade, and R. Hanson, High-fidelity projective read-out of a solid-state spin quantum register, Nature (London) 477, 574 (2011).
- [7] P. C. Humphreys, N. Kalb, J. P. J. Morits, R. N. Schouten, R. F. L. Vermeulen, D. J. Twitchen, M. Markham, and R. Hanson, Deterministic delivery of remote entanglement on a quantum network, Nature (London) 558, 268 (2018).
- [8] A. Jarmola, V. M. Acosta, K. Jensen, S. Chemerisov, and D. Budker, Temperature- and Magnetic-Field-Dependent Longitudinal Spin Relaxation in Nitrogen-Vacancy Ensembles in Diamond, Phys. Rev. Lett. 108, 197601 (2012).
- [9] T. Astner, J. Gugler, A. Angerer, S. Wald, S. Putz, N. J. Mauser, M. Trupke, H. Sumiya, S. Onoda, J. Isoya, J. Schmiedmayer, P. Mohn, and J. Majer, Solid-state electron spin lifetime limited by phononic vacuum modes, Nat. Mater. 17, 313 (2018).
- [10] N. Zhao, J. Honert, B. Schmid, M. Klas, J. Isoya, M. Markham, D. Twitchen, F. Jelezko, R.-B. Liu, H. Fedder, and J. Wrachtrup, Sensing single remote nuclear spins, Nat. Nanotechnol. 7, 657 (2012).
- [11] N. Bar-Gill, L. M. Pham, A. Jarmola, D. Budker, and R. L. Walsworth, Solid-state electronic spin coherence time approaching one second, Nat. Commun. 4, 1743 (2013).
- [12] D. D. Awschalom, R. Hanson, J. Wrachtrup, and B. B. Zhou, Quantum technologies with optically interfaced solid-state spins, Nat. Photonics 12, 516 (2018).
- [13] L. C. Bassett, A. Alkauskas, A. L. Exarhos, and K.-M. C. Fu, Quantum defects by design, Nanophotonics 8, 1867 (2019).
- [14] C. G. Yale, B. B. Buckley, D. J. Christle, G. Burkard, F. J. Heremans, L. C. Bassett, and D. D. Awschalom, All-optical control of a solid-state spin using coherent dark states, Proc. Natl. Acad. Sci. 110, 7595 (2013).
- [15] G. D. Fuchs, V. V. Dobrovitski, D. M. Toyli, F. J. Heremans, and D. D. Awschalom, Gigahertz dynamics of a strongly driven single quantum spin, Science 326, 1520 (2009).
- [16] W. F. Koehl, B. B. Buckley, F. J. Heremans, G. Calusine, and D. D. Awschalom, Room temperature coherent control of defect spin qubits in silicon carbide, Nature (London) 479, 84 (2011).
- [17] M. Widmann, S.-Y. Lee, T. Rendler, N. T. Son, H. Fedder, S. Paik, L.-P. Yang, N. Zhao, S. Yang, I. Booker, A. Denisenko, M. Jamali, S. A. Momenzadeh, I. Gerhardt, T. Ohshima, A. Gali, E. Janzén, and J. Wrachtrup, Coherent control of single spins in silicon carbide at room temperature, Nat. Mater. 14, 164 (2015).
- [18] Ö. O. Soykal, P. Dev, and S. E. Economou, Silicon vacancy center in 4*h*-sic: Electronic structure and spin-photon interfaces, Phys. Rev. B **93**, 081207(R) (2016).
- [19] M. Bockstedte, F. Schütz, T. Garratt, V. Ivády, and A. Gali, Ab initio description of highly correlated states in defects for realizing quantum bits, npj Quantum Mater. 3, 31 (2018).
- [20] R. Nagy, M. Niethammer, M. Widmann, Y.-C. Chen, P. Udvarhelyi, C. Bonato, J. U. Hassan, R. Karhu, I. G. Ivanov, N. T. Son, J. R. Maze, T. Ohshima, Ö. O. Soykal, Á. Gali, S.-Y. Lee, F. Kaiser, and J. Wrachtrup, High-fidelity spin and optical control of single silicon-vacancy centres in silicon carbide, Nat. Commun. 10, 1954 (2019).
- [21] A. M. Edmonds, M. E. Newton, P. M. Martineau, D. J. Twitchen, and S. D. Williams, Electron paramagnetic resonance studies of silicon-related defects in diamond, Phys. Rev. B 77, 245205 (2008).

- [22] A. Gali and J. R. Maze, Ab initio study of the split siliconvacancy defect in diamond: Electronic structure and related properties, Phys. Rev. B **88**, 235205 (2013).
- [23] B. Pingault, D.-D. Jarausch, C. Hepp, L. Klintberg, J. N. Becker, M. Markham, C. Becher, and M. Atatüre, Coherent control of the silicon-vacancy spin in diamond, Nat. Commun. 8, 15579 (2017).
- [24] B. C. Rose, D. Huang, Z.-H. Zhang, P. Stevenson, A. M. Tyryshkin, S. Sangtawesin, S. Srinivasan, L. Loudin, M. L. Markham, A. M. Edmonds, D. J. Twitchen, S. A. Lyon, and N. P. de Leon, Observation of an environmentally insensitive solid-state spin defect in diamond, Science 361, 60 (2018).
- [25] H. Ma, M. Govoni, and G. Galli, Quantum simulations of materials on near-term quantum computers, npj Comput. Mater. 6, 85 (2020).
- [26] C. Yin, M. Rancic, G. G. de Boo, N. Stavrias, J. C. McCallum, M. J. Sellars, and S. Rogge, Optical addressing of an individual erbium ion in silicon, Nature (London) 497, 91 (2013).
- [27] T. Kornher, D.-W. Xiao, K. Xia, F. Sardi, N. Zhao, R. Kolesov, and J. Wrachtrup, Sensing Individual Nuclear Spins with a Single Rare-Earth Electron Spin, Phys. Rev. Lett. 124, 170402 (2020).
- [28] A. Gali, M. Fyta, and E. Kaxiras, Ab initio supercell calculations on nitrogen-vacancy center in diamond: Electronic structure and hyperfine tensors, Phys. Rev. B 77, 155206 (2008).
- [29] A. Lenef and S. C. Rand, Electronic structure of the n-v center in diamond: Theory, Phys. Rev. B 53, 13441 (1996).
- [30] N. B. Manson, J. P. Harrison, and M. J. Sellars, Nitrogenvacancy center in diamond: Model of the electronic structure and associated dynamics, Phys. Rev. B 74, 104303 (2006).
- [31] L. J. Rogers, S. Armstrong, M. J. Sellars, and N. B. Manson, Infrared emission of the NV center in diamond: Zeeman and uniaxial stress studies, New J. Phys. **10**, 103024 (2008).
- [32] V. M. Acosta, A. Jarmola, E. Bauch, and D. Budker, Optical properties of the nitrogen-vacancy singlet levels in diamond, Phys. Rev. B **82**, 201202(R) (2010).
- [33] A. Batalov, C. Zierl, T. Gaebel, P. Neumann, I.-Y. Chan, G. Balasubramanian, P. R. Hemmer, F. Jelezko, and J. Wrachtrup, Temporal Coherence of Photons Emitted by Single Nitrogen-Vacancy Defect Centers in Diamond Using Optical Rabi-Oscillations, Phys. Rev. Lett. 100, 077401 (2008).
- [34] D. M. Toyli, D. J. Christle, A. Alkauskas, B. B. Buckley, C. G. Van de Walle, and D. D. Awschalom, Measurement and Control of Single Nitrogen-Vacancy Center Spins Above 600 k, Phys. Rev. X 2, 031001 (2012).
- [35] P. Kehayias, M. W. Doherty, D. English, R. Fischer, A. Jarmola, K. Jensen, N. Leefer, P. Hemmer, N. B. Manson, and D. Budker, Infrared absorption band and vibronic structure of the nitrogenvacancy center in diamond, Phys. Rev. B 88, 165202 (2013).
- [36] M. L. Goldman, A. Sipahigil, M. W. Doherty, N. Y. Yao, S. D. Bennett, M. Markham, D. J. Twitchen, N. B. Manson, A. Kubanek, and M. D. Lukin, Phonon-Induced Population Dynamics and Intersystem Crossing in Nitrogen-Vacancy Centers, Phys. Rev. Lett. 114, 145502 (2015).
- [37] M. L. Goldman, M. W. Doherty, A. Sipahigil, N. Y. Yao, S. D. Bennett, N. B. Manson, A. Kubanek, and M. D. Lukin, Erratum: State-selective intersystem crossing in nitrogen-vacancy centers [Phys. Rev. B 91, 165201 (2015)], Phys. Rev. B 96, 039905(E) (2017).

- [38] P. Delaney, J. C. Greer, and J. A. Larsson, Spin-polarization mechanisms of the nitrogen-vacancy center in diamond, Nano Lett. **10**, 610 (2010).
- [39] J. P. Goss, R. Jones, S. J. Breuer, P. R. Briddon, and S. Öberg, The Twelve-Line 1.682 ev Luminescence Center in Diamond and the Vacancy-Silicon Complex, Phys. Rev. Lett. 77, 3041 (1996).
- [40] A. S. Zyubin, A. M. Mebel, M. Hayashi, H. C. Chang, and S. H. Lin, Quantum chemical modeling of photoadsorption properties of the nitrogen-vacancy point defect in diamond, J. Comput. Chem. 30, 119 (2009).
- [41] C.-K. Lin, Y.-H. Wang, H.-C. Chang, M. Hayashi, and S. H. Lin, One- and two-photon absorption properties of diamond nitrogen-vacancy defect centers: A theoretical study, J. Chem. Phys. 129, 124714 (2008).
- [42] G. Davies, M. F. Hamer, and W. C. Price, Optical studies of the 1.945 ev vibronic band in diamond, Proc. R. Soc. London A 348, 285 (1976).
- [43] Y. Ma, M. Rohlfing, and A. Gali, Excited states of the negatively charged nitrogen-vacancy color center in diamond, Phys. Rev. B 81, 041204(R) (2010).
- [44] S. Choi, M. Jain, and S. G. Louie, Mechanism for optical initialization of spin in nv⁻ center in diamond, Phys. Rev. B 86, 041202(R) (2012).
- [45] J. P. Perdew, K. Burke, and Y. Wang, Generalized gradient approximation for the exchange-correlation hole of a manyelectron system, Phys. Rev. B 54, 16533 (1996).
- [46] P. Giannozzi, O. Andreussi, T. Brumme, O. Bunau, M. B. Nardelli, M. Calandra, R. Car, C. Cavazzoni, D. Ceresoli, M. Cococcioni, N. Colonna, I. Carnimeo, A. D. Corso, S. de Gironcoli, P. Delugas, R. A. DiStasio, A. Ferretti, A. Floris, G. Fratesi, G. Fugallo, R. Gebauer, U. Gerstmann, F. Giustino, T. Gorni, J. Jia, M. Kawamura, H.-Y. Ko, A. Kokalj, E. Küçükbenli, M. Lazzeri, M. Marsili, N. Marzari, F. Mauri, N. L. Nguyen, H.-V. Nguyen, A. O. de-la Roza, L. Paulatto, S. Poncé, D. Rocca, R. Sabatini, B. Santra, M. Schlipf, A. P. Seitsonen, A. Smogunov, I. Timrov, T. Thonhauser, P. Umari, N. Vast, X. Wu, and S. Baroni, Advanced capabilities for materials modeling with quantum ESPRESSO, J. Phys.: Condens. Matter 29, 465901 (2017).
- [47] V. Ivády, T. Simon, J. R. Maze, I. A. Abrikosov, and A. Gali, Pressure and temperature dependence of the zero-field splitting in the ground state of nv centers in diamond: A first-principles study, Phys. Rev. B 90, 235205 (2014).
- [48] B. O. Roos, R. Lindh, P. Å. Malmqvist, V. Veryazov, and P.-O. Widmark, *Multiconfigurational Quantum Chemistry* (John Wiley & Sons, Hoboken, New Jersey, 2016).
- [49] I. Fdez. Galván, M. Vacher, A. Alavi, C. Angeli, F. Aquilante, J. Autschbach, J. J. Bao, S. I. Bokarev, N. A. Bogdanov, R. K. Carlson, L. F. Chibotaru, J. Creutzberg, N. Dattani, M. G. Delcey, S. S. Dong, A. Dreuw, L. Freitag, L. M. Frutos, L. Gagliardi, F. Gendron, A. Giussani, L. González, G. Grell, M. Guo, C. E. Hoyer, M. Johansson, S. Keller, S. Knecht, G. Kovačević, E. Källman, G. Li Manni, M. Lundberg, Y. Ma, S. Mai, J. P. Malhado, P. Å. Malmqvist, P. Marquetand, S. A. Mewes, J. Norell, M. Olivucci, M. Oppel, Q. M. Phung, K. Pierloot, F. Plasser, M. Reiher, A. M. Sand, I. Schapiro, P. Sharma, C. J. Stein, L. K. Sørensen, D. G. Truhlar, M. Ugandi, L. Ungur, A. Valentini, S. Vancoillie, V. Veryazov, O. Weser, T. A. Wesołowski, P.-O. Widmark, S. Wouters, A. Zech, J. P.

- Zobel, and R. Lindh, Openmolcas: From source code to insight, J. Chem. Theory Comput. **15**, 5925 (2019).
- [50] F. Neese, Software update: The orca program system, version 4.0, WIREs Comput. Mol. Sci. 8, e1327 (2018).
- [51] F. Neese, The orca program system, WIREs Comput. Mol. Sci. 2, 73 (2012).
- [52] T. H. Dunning, Gaussian basis sets for use in correlated molecular calculations. I. The atoms boron through neon and hydrogen, J. Chem. Phys. 90, 1007 (1989).
- [53] W. A de Jong, R. J. Harrison, and D. A. Dixon, Parallel douglas-kroll energy and gradients in nwchem: Estimating scalar relativistic effects using douglas-kroll contracted basis sets, J. Chem. Phys. 114, 48 (2001).
- [54] J. R. Maze, A. Gali, E. Togan, Y. Chu, A. Trifonov, E. Kaxiras, and M. D. Lukin, Properties of nitrogen-vacancy centers in diamond: the group theoretic approach, New J. Phys. 13, 025025 (2011).
- [55] M. W. Doherty, N. B. Manson, P. Delaney, and L. C. L. Hollenberg, The negatively charged nitrogen-vacancy center in diamond: the electronic solution, New J. Phys. 13, 025019 (2011).
- [56] G. Kovačević and V. Veryazov, Luscus: Molecular viewer and editor for molcas, J. Cheminform. 7, 16 (2015).
- [57] K. Andersson and B. O. Roos, Excitation energies in the nickel atom studied with the complete active space scf method and second-order perturbation theory, Chem. Phys. Lett. 191, 507 (1992).
- [58] B. O. Roos, K. Andersson, M. P. Fülscher, P. Å. Malmqvist, L. Serrano-Andrés, K. Pierloot, and M. Merchán, Multiconfigurational perturbation theory: Applications in electronic spectroscopy, in *Advances in Chemical Physics*, edited by I. Prigogine and S. A. Rice (John Wiley & Sons, Ltd, 1996), pp. 219–331.
- [59] Q. M. Phung, S. Vancoillie, and K. Pierloot, A multiconfigurational perturbation theory and density functional theory study on the heterolytic dissociation enthalpy of first-row metallocenes, J. Chem. Theory Comput. 8, 883 (2012).
- [60] C. J. Stein, V. von Burg, and M. Reiher, The delicate balance of static and dynamic electron correlation, J. Chem. Theory Comput. 12, 3764 (2016).
- [61] B. A. Hess, C. M. Marian, U. Wahlgren, and O. Gropen, A mean-field spin-orbit method applicable to correlated wavefunctions, Chem. Phys. Lett. 251, 365 (1996).
- [62] P. Å. Malmqvist, B. O. Roos, and B. Schimmelpfennig, The restricted active space (ras) state interaction approach with spin–orbit coupling, Chem. Phys. Lett. 357, 230 (2002).
- [63] F. Neese, Importance of direct spin–spin coupling and spinflip excitations for the zero-field splittings of transition metal complexes: A case study, J. Am. Chem. Soc. 128, 10213 (2006).
- [64] G. Barcza, V. Ivády, T. Szilvási, M. Vörös, L. Veis, Ádám Gali, and Örs Legeza, DMRG on top of plane-wave Kohn-Sham orbitals: A Case Study of defected boron nitride, J. Chem. Theory Comput. (2021), doi: 10.1021/acs.jctc.0c00809.
- [65] J. A. Larsson and P. Delaney, Electronic structure of the nitrogen-vacancy center in diamond from first-principles theory, Phys. Rev. B 77, 165201 (2008).
- [66] Ádám Gali, Ab initio theory of the nitrogen-vacancy center in diamond, Nanophotonics **8**, 1907 (2019).

- [67] P. Tamarat, N. B. Manson, J. P. Harrison, R. L. McMurtrie, A. Nizovtsev, C. Santori, R. G. Beausoleil, P. Neumann, T. Gaebel, F. Jelezko, P. Hemmer, and J. Wrachtrup, Spin-flip and spin-conserving optical transitions of the nitrogen-vacancy center in diamond, New J. Phys. 10, 045004 (2008).
- [68] A. Batalov, V. Jacques, F. Kaiser, P. Siyushev, P. Neumann, L. J. Rogers, R. L. McMurtrie, N. B. Manson, F. Jelezko, and J. Wrachtrup, Low Temperature Studies of the Excited-State Structure of Negatively Charged Nitrogen-Vacancy Color Centers in Diamond, Phys. Rev. Lett. 102, 195506 (2009).
- [69] K.-M. C. Fu, C. Santori, P. E. Barclay, L. J. Rogers, N. B. Manson, and R. G. Beausoleil, Observation of the Dynamic

- Jahn-Teller Effect in the Excited States of Nitrogen-Vacancy Centers in Diamond, Phys. Rev. Lett. **103**, 256404 (2009).
- [70] T. A. Abtew, Y. Y. Sun, B.-C. Shih, P. Dev, S. B. Zhang, and P. Zhang, Dynamic Jahn-Teller Effect in the nv⁻ Center in Diamond, Phys. Rev. Lett. 107, 146403 (2011).
- [71] F. S. Ham, Effect of linear jahn-teller coupling on paramagnetic resonance in a 2e state, Phys. Rev. **166**, 307 (1968).
- [72] Gergő Thiering and A. Gali, Ab initio calculation of spin-orbit coupling for an nv center in diamond exhibiting dynamic jahnteller effect, Phys. Rev. B **96**, 081115(R) (2017).
- [73] J. Marcus and V. Veryazov, Automatic procedure for generating symmetry adapted wavefunctions, J. Cheminform. 9, 8 (2017).